Wind-Tunnel Experiment of Heavy Gas and Passive Scalar Emission in a Turbulent Boundary Layer

Original
Wind-Tunnel Experiment of Heavy Gas and Passive Scalar Emission in a Turbulent Boundary Layer / Vidali, C.; Marro, M.; Gostiaux, L.; Houssin, D.; Vyazmina, E.; Salizzoni, P.. - In: BOUNDARY-LAYER METEOROLOGY. - ISSN 1573-1472. - 191:4(2025). [10.1007/s10546-025-00909-w]

Publisher:
Springer Nature

Published
DOI:10.1007/s10546-025-00909-w

Boundary-Layer Meteorology (2025) 191:18
https://doi.org/10.1007/s10546-025-00909-w

RESEARCH ARTICLE

Wind-Tunnel Experiment of Heavy Gas and Passive Scalar Emission in a Turbulent Boundary Layer

Cristina Vidali[1,2] · **Massimo Marro**[1] · **Louis Gostiaux**[1] · **Deborah Houssin**[2] ·
Elena Vyazmina[2] · **Pietro Salizzoni**[1,3]

Received: 12 August 2024 / Accepted: 20 February 2025 / Published online: 22 March 2025

Abstract

The aim of this study is to experimentally investigate the dynamics of a heavy gas release and highlight its main differences compared to that of a passive gas. To achieve this, we examine the vertical emission of both heavy and passive gases from an elevated source, situated within a turbulent boundary layer. The wind tunnel experiment is designed to simulate a realistic release of oxygen at T = – 40 °C, following a similar setup to the study performed by Schatzmann et al. (Atmos Environ 27:1105–1116, 1993). The release is characterised by means of simultaneous velocity and concentration measurements along vertical and lateral profiles at various downwind distances from the source. The data were used to estimate the turbulent mass flows, the turbulent Schmidt number, and the high-order statistics of the scalar field. Furthermore, we conduct an in-depth analysis of the production and dissipation terms of the concentration variance. These are subsequently used to estimate the typical time scale for turbulent mixing using two different micro-mixing models that parametrize the effects of molecular diffusion. These findings are crucial for improving the accuracy of operational dispersion models that simulate localised releases of dense gases in the atmosphere.

Keywords Atmospheric turbulence · Concentration fluctuations · Heavy gas releases · Wind-tunnel experiments

1 Introduction

The management of risks associated with accidental releases of toxic or flammable heavy gases requires estimating the probability of exceeding given concentration thresholds at varying distances from the pollutant source. To achieve this, dispersion models capable of reproducing the one-point probability density function (PDF) (Bertagni et al. 2019; Cassiani et al. 2020) and the main features of their temporal evolution (Bertagni et al. 2020) are

---

✉ Massimo Marro
marro.massimo@ec-lyon.fr

[1] Ecole Centrale de Lyon, CNRS, INSA Lyon, LMFA, UMR5509, Universite Claude Bernard Lyon 1, 69130 Ecully, France

[2] Air Liquide Paris Research and Development Center, Paris Innovation Campus, 1 chemin de la Porte des Loges, Les Loges-en-Josas, Jouy-en-Josas, France

[3] Department of Environmental, Land, and Infrastructure Engineering, Politecnico di Torino, Corso Duca degli Abruzzi 24, 10129 Turin, Italy

essential. Developing these models is a challenging task, demanding a deep understanding of the physics involved in the dispersion and mixing of dense gas releases. The spreading of a plume of gases heavier than air creates stable stratified flow conditions that potentially inhibit the dispersion process. In the case of inflammable or toxic dense gases, reduced dilution with ambient air and stagnation close to ground level may lead to concentrations exceeding flammability and toxicity thresholds at larger distances from the emission source compared to light or passive releases. As a result, dense releases are generally associated with higher environmental risks.

Laboratory studies of atmospheric dense gas dispersion are typically conducted in wind tunnels, where these releases are often simulated using mixtures of air and carbon dioxide, CO_2 (Meroney 1982; Schatzmann et al. 1993; Snyder 2001; Briggs et al. 2001; Hanna and Chang 2001; Britter and Snyder 1988). Larger density differences can be obtained with mixtures of air and SF_6 (Schatzmann et al. 1993; König-Langlo and Schatzmann 1991) or freon (F. T. Bodurtha 1961; Hoot et al. 1973; Ayrault et al. 1991). However, the use of these substances has been restricted nowadays due to safety and environmental regulations.

Previous studies have primarily focused on experimentally characterizing the mean concentration field induced by dense gas releases from elevated and ground-level sources in neutrally stratified boundary layers (Meroney and Lohmeyer 1984; Heidorn et al. 1992; Britter 1989; Schatzmann et al. 1993; Donat and Schatzmann 1999). More recent investigations have extended this focus to consider the effects of obstacles (König-Langlo and Schatzmann 1991; Roberts and Hall 1994; Snyder 2001; Hanna and Steinberg 2001; Briggs et al. 2001; Zhu et al. 1998) and varying atmospheric stability conditions (Robins et al. 2001a, b). However, to our knowledge, only few studies have provided insights into higher-order statistics of gas concentration. For instance, Britter and Snyder (1988) used CO_2 to simulate a steady dense gas emission over a ramp and measured the concentration field's mean and standard deviation using a Flame Ionisation Detector (FID). Meroney and Lohmeyer (1984) examined the behaviour of suddenly released volumes of dense gas in a turbulent boundary layer, obtaining statistics on the mean concentration field, departure/arrival time, and concentration fluctuations by reproducing multiple cloud volumes. Ayrault et al. (1998) investigated the dispersion of an unsteady ground release and provided ensemble statistics of the first four moments of the concentration.

This literature review highlights a lack of experimental data on higher-order statistics of dense gas concentration and turbulent mass fluxes. To address this gap, we focus on the release of a vertical heavy gas plume from an elevated source in a turbulent boundary layer. The configuration is similar to the one investigated by Schatzmann et al. (1993) and Donat and Schatzmann (1999), aiming at reproducing a real-case scenario of O_2 emission at a temperature of $-40\,^{\circ}\mathrm{C}$.

In the following sections, we introduce the experimental setup and methods, describe the governing parameters of the dispersion process for heavy gas emissions, including the similarity condition between our experiment, the real-case scenario, and the Schatzmann et al. (1993) configuration (Sect. 2). After briefly presenting the mean features characterizing the velocity field, we discuss the spatial distribution of the one-point concentration statistics and the joint velocity-concentration statistics (Sect. 3). Conclusions are drawn in Sect. 4.

2 Experimental Methods

2.1 Governing Parameters and Similarity Conditions

We investigate the atmospheric dispersion of a heavy gas and a passive scalar emitted from an elevated source within a turbulent boundary layer. The source has a diameter d_s, height h_s, and releases a volume rate flow Q_s with a vertical emission velocity w_s. The turbulent boundary layer in which the emission takes place is the same as the one investigated by Nironi et al. (2015). Its characteristic scales, schematically shown in Fig. 1, include its depth δ, friction velocity u_*, and the free stream velocity U_∞.

In general, the concentration field can be considered as a function of the following governing parameters:

$$c = f(w_s, Q_s, \rho_a, \rho_s, h_s, d_s, \delta, U_\infty, u_*, \nu_a, \nu_s, D, g), \tag{1}$$

where D is the diffusivity of the gas mixture in air, g is the gravitational acceleration, ρ is the density, and ν is the viscosity. The subscripts ‘a’ and ‘s’ refer to ambient air and the dense gas at the source, respectively.

Rewriting Eq. 1 in dimensionless form, we have:

$$c^* = \frac{c}{\Delta c} = f\left(V_r, \frac{\rho_s}{\rho_a}, \frac{h_s}{\delta}, \frac{d_s}{\delta}, \frac{u_*}{U_\infty}, Re, Fr, Sc, Sc_s\right), \tag{2}$$

where c^* is the concentration normalised by a scale of the concentration variations, defined as:

$$\Delta c = Q_s \rho_s / (U_\infty \delta^2), \tag{3}$$

where $V_r = w_s / U_\infty$ is the ratio between the source and the boundary layer velocities, $Sc = \nu_a / D$ and $Sc_s = \nu_s / D$ are the Schmidt numbers of the flow and at the source location, respectively, Fr and Re are the Froude number (the ratio between inertial and buoyancy forces) and the Reynolds number (the ratio between inertial and viscosity forces), respectively. The definition of Fr and Re can be based on different scales, related to the boundary layer or to the source. The formulations for the Fr and Re numbers commonly adopted in the literature are reported in Table 1.

To achieve dynamical similarity between small-scale experiments and real scenarios, all non-dimensional parameters in Eq. 2 must, in principle, be kept constant. However, when replicating experiments with a reduced-scale model in a wind tunnel, it is impossible to maintain these conditions strictly. Specifically, fixing the Froude number, which is crucial for these experiments, leads to conflicts in reproducing realistic values for both the source Reynolds number and the geometrical ratio d_s/δ, which in reality are approximately 10^6 and 10^{-3}, respectively.

To address these constraints, it is generally accepted that dynamical similarity can still be achieved by reducing Re_s by one or two orders of magnitude, as long as the flow remains fully turbulent. For buoyant releases in a co-flow, the criterion by Arya and Lape (1990), is often adopted, which states that variations in Re_s do not affect plume dynamics above a critical value of 1500 for momentum-dominated plumes and around 600 for buoyancy-dominated plumes. Similarly, it is assumed that the dispersion process similarity can be maintained with a larger geometrical ratio than the real one, as long as there is a significant gap between the source diameter scale and the boundary layer height (Marro et al. 2014; Nironi et al. 2015), i.e. $d_s/\delta \sim 10^{-1} \div 10^{-2}$. This ensures that the initial plume size remains

Table 1 Formulations of the Froude and the Reynolds numbers based on the typical velocity and length scales referred to the source or the boundary layer flow

Name	Symbol	Definition
Source Froude number	Fr_s	$w_s/\sqrt{gd_s\frac{\rho_s-\rho_a}{\rho_s}}$
BL Froude number	Fr_∞	$U_\infty/\sqrt{gd_s\frac{\rho_s-\rho_a}{\rho_s}}$
Source Reynolds number	Re_s	$w_s d_s/\nu_s$
BL Reynolds number	Re_∞	$U_\infty\delta/\nu_a$

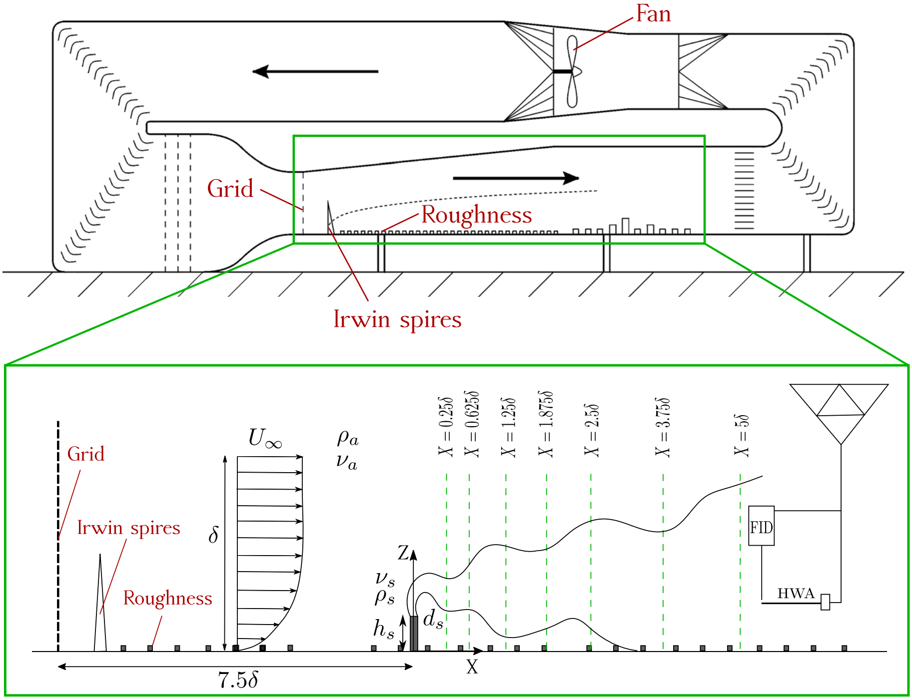

Fig. 1 The LMFA atmospheric wind tunnel with a scheme (not in scale) of the experimental setup of the source, the coupled measurements system, the measuring sections and the governing parameters

considerably smaller than the larger eddies in the boundary layer flow, effectively simulating the meandering motion typical in the early stages of pollutant plume dispersion in the lower atmosphere (Fackrell and Robins 1982).

2.2 Experimental Set-Up

Experiments were performed in the atmospheric wind tunnel of the Laboratoire de Mécanique des Fluides et d'Acoustique (LMFA) of the École Centrale de Lyon (France), a recirculating wind tunnel with a working section of 14 m long, 3.7 m wide and an adjustable ceiling (2−2.5 m) to control longitudinal pressure gradients (Fig. 1). The facility is regulated in temperature, to limit the temperature variations during a one-day experiment in the range ± 0.5 °C.

We generated a neutral turbulent boundary layer by means of floor roughness combined with a grid and a row of spires (Nironi et al. 2015) placed at the entrance of the test section

Table 2 Governing parameters: experimental set-up versus Schatzmann et al. (1993)

Name	Symbol	Experiments		Schatzmann	
		Value	Units	Value	Units
Boundary layer height	δ	0.8	m	1	m
Boundary layer velocity	U_∞	1.45	m/s	1.32	m/s
Source velocity	w_s	2.37	m/s	4.58	m/s
Source height	h_s	76	mm	76.2	mm
Source diameter	d_s	12	mm	6.35	mm
Velocity Ratio	V_r	1.63	[–]	3.47	[–]
Density ratio	ρ_s/ρ_a	1.5	[–]	1.56	[–]
Source Froude number	Fr_s	16.15	[–]	30.6	[–]
BL Froude number	Fr_∞	12	[–]	7.06	[–]
Source Reynolds number CO_2	Re_{s,CO_2}	3.4×10^3	[–]	3.6×10^3	[–]
Source Reynolds number passive scalar	$Re_{s,p}$	1.8×10^3	[–]	3.6×10^3	[–]
BL Reynolds number	Re_∞	7.63×10^4	[–]	8.69×10^4	[–]
BL velocity ratio	u_*/U_∞	0.04	[–]	n.a	[–]
Source Schmidt number	Sc_s	0.50	[–]	n.a	[–]
Flow Schmidt number	Sc	0.95	[–]	n.a	[–]

(Fig. 1). The roughness elements on the floor are equally spaced cubes of height $h_r = 0.02$ m, simulating a typical rural site roughness. The grid at the entrance is used to stabilise the flow and to reduce inhomogeneities in the transverse direction. The Irwin spires (Irwin 1981) are $H = 0.5$ m high and spaced by $H/2$. A fully turbulent flow is created imposing a free stream velocity $U_\infty = 1.45$ m/s, the resultant boundary layer height is $\delta = 0.8$ m and the corresponding Reynolds number $Re_\infty = U_\infty \delta/\nu_a \approx 7.63 \times 10^4$ (Table 1), where $\nu_a = 1.51 \times 10^{-5}$ m^2/s is the the air kinematic viscosity at $T = 20\,°C$. As observed in Nironi et al. (2015), the wind tunnel flow drifts in the transverse direction slightly less than 2%.

The studied configuration is a scale model for the real case scenario of the emission of oxygen O_2 at T = – 40 °C, i.e. characterised by a density ratio $\rho_s/\rho_a = 1.5$. The geometric scaling, between the wind tunnel and the real case scenario, is set on a ratio of 1 : 100. Imposing the similarity on the Fr_s, the resulting velocities scales by a factor 1 : 10. To simulate this release, we use carbon dioxide as a buoyant agent, emitted in a mixture with air and ethane, the latter used as a tracer for concentration measurements (see Sect. 2.3). At $T = 20\,°C$, the density values are 1.8 kg/m^3 for the CO_2 and about 1.2 kg/m^3 for both ethane and air.

The experiment set-up presents several similarities with the configuration studied by Schatzmann et al. (1993), notably with the one referred to as "3T". Compared to the case studied by Schatzmann et al. (1993), both source size and the emission velocity are different, and set to reduce the Froude number at the source Fr_s, i.e. to maximise the buoyancy at the source and its effects on the plume dynamics. The parameters of our experimental set-up and the corresponding ones by Schatzmann et al. (1993) are reported in Table 2.

The source is made of a metallic pipe of internal diameter $d_s = 0.012$ m and height $h_s = 0.075$ m from ground level and the gas mixture is emitted with a vertical velocity of $w_s = 2.37$ m/s, giving $V_r = w_s/U_\infty = 1.63$. The Froude number at the source is then $Fr_s \approx 16$ while the Reynolds number at the source is $Re_{s,CO_2} = 3.4 \times 10^3$ (the CO_2

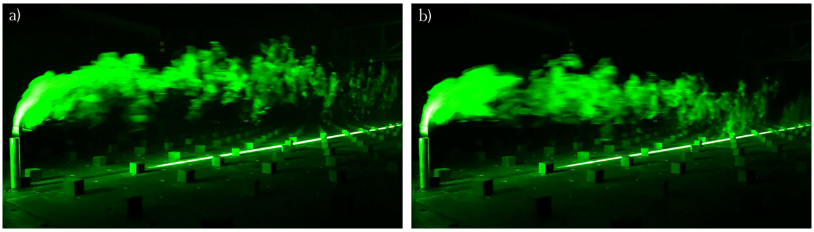

Fig. 2 Laser tomographic visualisation of **a** the passive scalar and **b** the heavy gas plume, under the same experimental emission and flow conditions

kinematic viscosity is $\nu_{CO_2} = 8.6 \times 10^{-6}$ m^2/s). Based on the boundary layer scales these two parameters are equal to $Fr_\infty \approx 12$ and $Re_\infty = 7.63 \times 10^4$, respectively (Table 1). The source is placed at 7.5δ from the beginning of the working section (Fig. 1), where the boundary layer can be considered fully developed (Nironi et al. 2015), so that the velocity statistics can be considered as dependent on z only (except within the roughness sub-layer). The origin of the coordinate system is the base of source, with x, y, and z as the longitudinal, transverse and vertical axes, respectively. We define the measurement sections for both vertical and transverse profiles at increasing distance from the source, as schematically reported in Fig. 1.

The passive scalar emission consists in a mixture of air and ethane and, therefore, there are no density differences with the ambient air. This release occurs within the same external boundary layer under and the source velocity ratio is kept equal to $V_r = 1.63$. This conditions determines a different value of $Re_{s,p} = 1.8 \times 10^3$, as the values of kinematic viscosity are different for air and CO$_2$.

The reference experiments by Arya and Lape (1990) demonstrated that, for a plume dispersing within a uniform flow with very low turbulence intensity ($< 1\%$), the first- and second-order statistics of the velocity field exhibited minimal sensitivity for $Re_s > 1.5 \times 10^3$. Based on these findings, we do not expect our results to be influenced by the Reynolds number at the source, either in terms of velocity or concentration statistics. Furthermore, the threshold value of $Re_s > 1.5 \times 10^3$ established by Arya and Lape (1990) specifically pertains to a non-turbulent external flow. This threshold can reasonably be expected to be lower for releases in flows with high turbulence intensity, such as the turbulent boundary layer considered in this study.

A qualitative overview of two releases is provided in Fig. 2, showing Laser tomographic visualisations of the heavy gas and passive scalar plumes. To perform the visualizations, we generated a vertical plane positioned at the centre of the plume using a 5 W laser. The flow was seeded with olive oil, introduced via an atomizer that produced polydisperse droplets with a typical diameter of about 1 μm (Marro et al. 2020).

As can be observed, the trajectories of the two plumes are different, with the heavy gas plume impacting the ground closer to the source.

2.3 Measurement Techniques

To fully characterise the plume concentrations and joint velocity-concentration statistics we combine two measurement techniques. Concentration measurements are performed with a Flame Ionization Detector (FID), with a sampling tube 0.3 m long, permitting a frequency response of 400 Hz. In case of heavy gas experiments, the instruments response is influenced by the presence of CO$_2$ and a specific calibration procedure is established and repeated twice a day. For an exhaustive description of the calibration procedure the reader is referred to (Vidali et al. 2022). Velocity measurements are performed with a X-Probe hot-wire anemometry with constant temperature that provides simultaneous measurements of two velocity components. In our set-up, the HWA has a frequency response of about 5 kHz. The response of the HWA is corrected taking into account the local CO_2 concentration in the calibration procedure. Since the experiments are conducted in a recirculating wind tunnel, the increase in background concentration over time must be evaluated throughout the entire daily experimental session.

Combined FID and HWA (Fig. 1) provided simultaneous measurements of concentration and velocity. Following Marro et al. (2020), the spacing between the FID and the LDA measurement volume were spaced by 5 mm. The frequency of the velocity-concentration signals is imposed by the FID sampling frequency. The combined HWA-FID system is therefore able to provide a signal for the joint statistics of concentration and velocity of 400 Hz, the one imposed by the frequency response of the FID. As widely discussed by Vidali et al. (2022), the main hurdle using this system is that the instruments responses vary with the ratio r between carbon dioxide and ethane, which has therefore to be taken into account in the calibration procedure. For further details on the latter and on the uncertainties related to our experimental estimates is provided in Vidali et al. (2022). Concentration and velocity statistics are performed on signals collected over 300 s.

3 Results

The dispersion process takes place within a turbulent boundary layer which is the same presented in Nironi et al. (2015). The only difference is related to a reduction of the free-stream velocity U_∞ which is here smaller than that imposed in Nironi et al. (2015) (1.45 m/s instead of 5.0 m/s), in order to maximise buoyancy effects (i.e. minimise the Froude number). As shown in Fig. 3, the reduced U_∞ (and therefore the reduced Reynolds number of the flow) has however no relevant effects on the normalised first- (Fig. 3a) and second-order statistics (Fig. 3b and c), whose vertical profiles are in very good agreement with those presented by Nironi et al. (2015). We can therefore assume that the flow is Reynolds independent and can be suitably modelled as a turbulent boundary layer, whose main features are here briefly summarised. In the lower part of the domain, the mean velocity profiles is well fitted by a logarithmic law:

$$\frac{\overline{u}(z)}{u_*} = \frac{1}{\kappa} \ln\left(\frac{z-d}{z_0}\right), \tag{4}$$

with $\kappa = 0.4$ the Von Karman constant. The friction velocity was computed from the Reynolds stress profile as $u_* = \sqrt{-\overline{u'w'}}$, averaging the $\overline{u'w'}$ values in the lower part of the flow field, where they vary minimally (Fig. 3c). The estimated value of the friction velocity was $u_* = 0.058$ m/s, implying a same ratio $u_*/U_\infty = 0.04$ as in Nironi et al. (2015). A boundary layer thickness of approximately $\delta \approx 0.8$ m was determined from the $\overline{u'w'}$ profile as the height where $d\overline{u'w'}/dz \approx 0$. The other parameters were determined by fitting the lower part of the mean velocity profile to the logarithmic law. We obtained $z_0 = 1.13 \times 10^{-4}$ m as surface roughness and $d = 0.013$ m as displacement height.

A good fit of the mean velocity profile $\overline{u}(z)$ in the whole turbulent boundary layer is instead provided by the power law:

$$\frac{\overline{u}(z)}{U_\infty} = \left(\frac{z}{\delta}\right)^n, \tag{5}$$

with $n = 0.23$ (Nironi et al. 2015).

As expected in a typical boundary layer flow, the velocity field is characterised by an equilibrium (see Fig. 3d) between the production $P_K \approx \overline{u'w'}\frac{\partial \overline{u}}{\partial z}$ and dissipation rate ε of the turbulent kinetic energy $K = \frac{1}{2}(\sigma_u^2 + \sigma_v^2 + \sigma_w^2)$ (TKE), the latter being estimated as:

$$\varepsilon_{iso} = \frac{15\nu}{\overline{u}^2}\overline{\left(\frac{\partial u'}{\partial t}\right)^2}, \tag{6}$$

i.e., assuming Taylor's hypothesis of frozen turbulent and the local isotropy of the velocity field (Hinze 1975).

In what follows, all quantities are presented in non-dimensional form (denoted with the symbol "*"), using U_∞, δ and Δc (see Eq. 3) as velocity, length, and concentration scale, respectively. In analysing profiles of the concentration statistics, we will systematically compare the case of the heavy release with that of the passive scalar one. We first analyse the mean concentration profiles $\overline{c*} = \frac{1}{N}\sum_{i=1}^{N} c_i^*$ (N is the sample size) for both the vertical and transverse section, and we present the parameters that characterise the time-averaged plume, such as the height of the centre of mass (Z_{MC}^*) and the vertical and transverse spreads (σ_z^* and σ_y^*, Sect. 3.1). We then consider the high-order moments of concentration, computed as:

$$m_{nc}^* = \left[\frac{1}{N}\sum_{i=1}^{N}\left(c_i^* - \overline{c^*}\right)^n\right]^{1/n}, \tag{7}$$

with $n = 2, 3, 4$, and analyse their link with the form of the one-point PDF (Sect. 3.2). The turbulent mass fluxes and the estimates of the turbulent dispersion coefficient are reported in Sect. 3.3. The analysis of the terms composing the balance equation of concentration variance is presented in Sect. 3.4. Finally, in Sect. 3.5, we present the estimate of the mixing timescale using different methods and compare the results with a theoretical model.

3.1 Mean Concentration Field

Figure 4a shows the vertical profiles of the mean concentration over sections at increasing distances from the source. As expected, the mean concentration decreases downstream from the source, which implies a rapid decrease of $\Delta\rho/\rho_a$ (i.e. of the relative density difference between the plume and ambient air). With a density difference at the source equal to 48.8%, the maximum of $\Delta\rho/\rho_a$ in the first measurement section is around 3%, and in the second decreases to almost 1%. These profiles enlighten the deflection of the heavy gas plume, which implies that, at the furthest profile close to the ground, $\overline{c*}$ is consistently higher for the heavy gas emission.

Figure 4b shows instead the transverse mean concentration profiles. These have been measured at the height at which the vertical concentration profiles shows a maximum. Therefore, statistics of passive and heavy gas transverse profiles are measured at different heights. The concentrations of both heavy and passive plume decrease as the distance from the source increases. As for the vertical profiles, the maxima of concentration in the first two sections are higher for the passive scalar release.

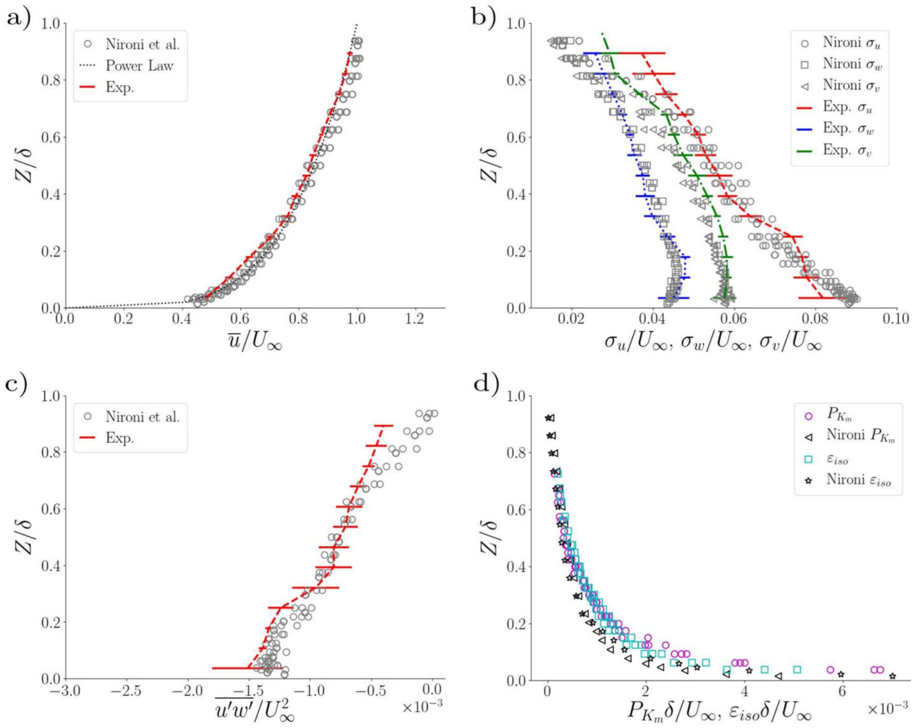

Fig. 3 **a** Vertical mean velocity profile, **b** standard deviation of horizontal, vertical and transverse velocity, **c** Reynolds stress, **d** TKE production P_k and dissipation rate ε, compared to benchmark Nironi et al. (2015)

As customary, the vertical and transverse mean concentration profiles can be suitably modelled by mean of a Gaussian model, taking into account an extra term to reproduce the effect of the reflection of the ground (Hay and Pasquill 1959):

$$\begin{aligned}\overline{c}(x,z) &= \frac{Q_s\rho_s}{2\pi\sigma_y\sigma_z\overline{u}_{MC}}\exp\left(-\frac{y^2}{2\sigma_y^2}\right)\\ &\quad\times\left[\exp\left(-\frac{(z-h_{eff})^2}{2\sigma_z^2}\right)+\exp\left(-\frac{(z+h_{eff})^2}{2\sigma_z^2}\right)\right],\end{aligned} \tag{8}$$

where $\overline{u}_{MC}$ is the mean longitudinal velocity at the centre of mass of the plume and $h_{eff} = h_s + \Delta h$ is the effective height of the plume estimated at each section, taking into account the plume rise Δh, as induced by the the vertical momentum flux imposed at the emission.

We fit the mean concentration profiles with the Eq. 8 and using σ_z and σ_y as free parameters (Fig. 4a and b). Resulting values of σ_z and σ_y are plotted in Fig. 5a, b, showing that there are no significant difference between the passive scalar and the heavy gas plumes in terms of vertical and transverse spread.

From the interpolation of the vertical profiles, we can also estimate the height of the centre of mass Z^*_{MC}, estimated as:

$$Z^*_{MC} = \frac{1}{\delta}\left(\frac{\int_0^\infty (c(z)\cdot z)dz}{\int_0^\infty c(z)dz}\right), \tag{9}$$

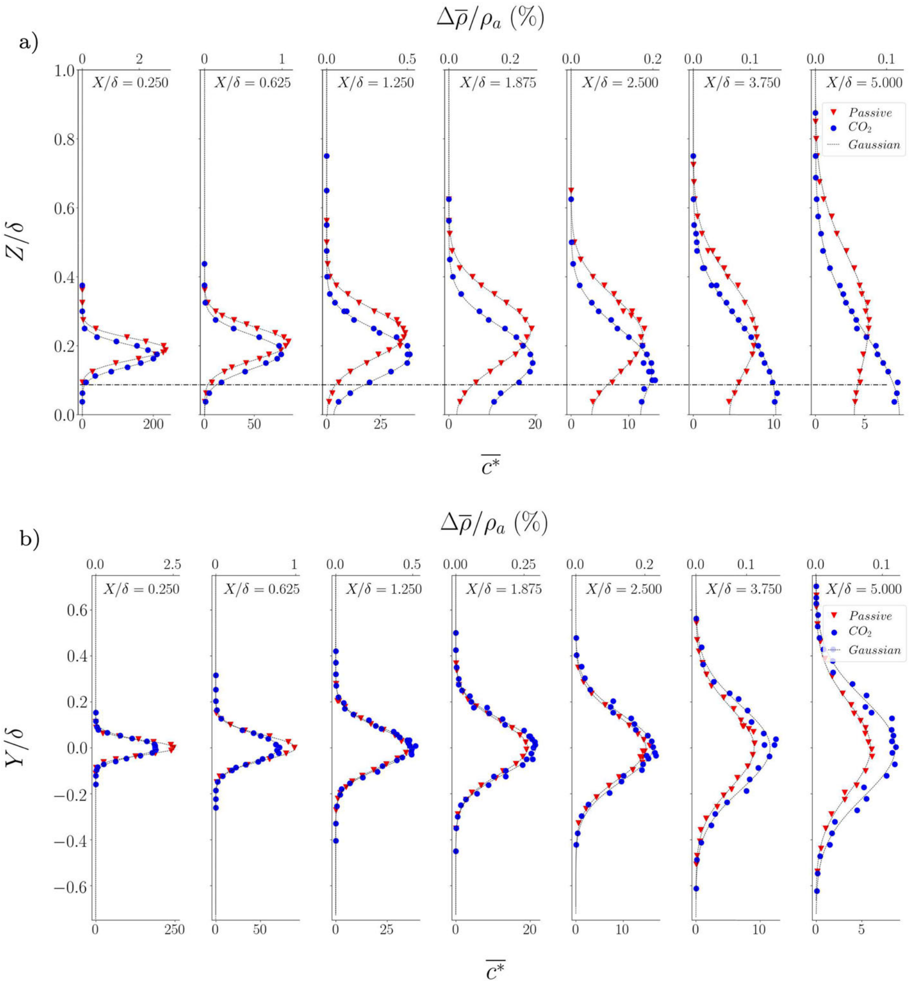

Fig. 4 Vertical **a** and transverse **b** profiles of the normalised mean concentration and dimensionless density difference for sections at increasing distance from the source for passive and heavy gas plume. The dashed line represents the position of the source height

and whose longitudinal evolution is plotted in Fig. 5c. In the near field, the role of buoyancy is to limit the height of the heavy gas plume. Notably, the negative buoyancy rapidly balances the effect of the vertical momentum flux imposed at the source, so that the Z_{MC} attains a local maximum close to the source and starts then to decrease. In the far field, once the plume attains the ground level, the height of the centre of mass tends to rise again, due to the vertical spread influenced by the reflection on the ground.

In Fig. 5a, b we also plot the values of σ_z and σ_y evaluated according the Taylor's formulation (Taylor 1922):

$$\sigma_z^2 = \frac{d_s^2}{6} + 2\sigma_w^2 T_{Lw} \left\{ t - T_{Lw} \left[1 - \exp\left(-\frac{t}{T_{Lw}} \right) \right] \right\}, \tag{10}$$

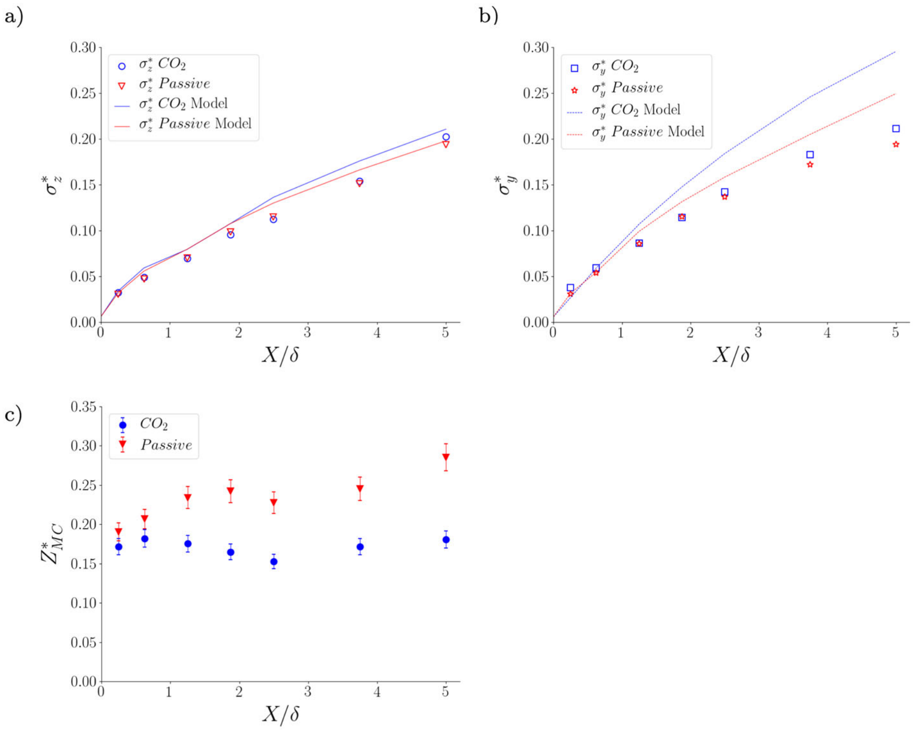

Fig. 5 Longitudinal profiles of **a** vertical and **b** transverse standard deviation compared with theoretical laws (Eqs. 10 and 11), **c** centre of mass height Z_{MC}^* for both heavy and passive scalar

$$\sigma_y^2 = \frac{d_s^2}{6} + 2\sigma_v^2 T_{Lv}\left\{t - T_{Lv}\left[1 - \exp\left(-\frac{t}{T_{Lv}}\right)\right]\right\}, \tag{11}$$

where t is the flight time, T_{Lw} and T_{Lv} are the Lagrangian time scales in the lateral and vertical direction, respectively, and estimated as (Tennekes and Lumley 1972):

$$T_{Lw} = \frac{2\sigma_w^2}{C_0\varepsilon}, \tag{12}$$

$$T_{Lv} = \frac{2\sigma_v^2}{C_0\varepsilon}, \tag{13}$$

where $C_0 = 4.5$ is the Kolmogorov constant (as estimated by Nironi et al. (2015) by comparing the Lagrangian length scales and the dissipation profiles). To take into account the effect of the in-homogeneity of the velocity field, the parameters σ_v, σ_w, T_{Lw}, and T_{Lv} are evaluated at the height of the centre of mass of the plume (which varies as the plume travels downstream). The flight time t is expressed as a function of the mean longitudinal velocity at Z_{MC} as $t = X/\overline{u}_{MC}$. It is worth noting that in this case the plume dynamics is notably complex, making the straightforward application of Eqs. 10 and 11 to both passive and dense scalars somewhat questionable. The high emission velocity relative to the external flow leads to a significant initial plume rise, with the centre of mass Z_{MC}^* shifting from $Z = 0.1\delta$ to $Z = 0.2\delta$ at the first measurement station. Subsequently, the negative buoyancy of the dense plume causes a reduction in Z_{MC}^*. This complexity is accounted for in Eqs. 10 and 11 through the evolving position of the plume centre of mass, only. This results in different flight times as well as different and turbulence quantities ($T_{Lv,w}$ and $\sigma_{v,w}$) seen by the passive and dense releases.

Despite these approximations, in Fig. 5a we observe a general good agreement between the experimental estimates of σ_z (i.e. obtained by fitting the experimental data with Eq. 8) and Taylor theoretical model (Eq. 10). Conversely, the transverse spreads σ_y computed with Eq. 11 are higher than the experimental estimates, especially in the heavy gas case. A similar discrepancy was also observed by Nironi et al. (2015), who studied the dispersion of a scalar emitted by an elevated L-shaped source in this same velocity field.

3.2 Higher Order Moments of the Concentration

The vertical and transverse profiles of the standard deviation σ_c^* are shown in Fig. 6a, b, respectively. As for the mean concentration field, the vertical profiles (Fig. 6a) of σ_c^* depict different trajectories of the two plumes, with the heavy gas plume deflected through the ground, compared to the passive scalar one. In the plume centre, σ_c^* is lower for the heavy gas, especially in the near field, where the effect of buoyancy on the plume dynamics is greatest. When considering transverse profiles (which, we recall, refer to different heights from the ground) shown in Fig. 6b, the different values of σ_c^* for the two plumes can be instead depicted only in the near field, i.e. along the first two sections.

Based on the values of $\overline{c^*}$ and σ_c^*, we can compute the intensity of the concentration fluctuation, denoted as $i_c = \sigma_c^*/\overline{c^*}$. Figure 7a shows the longitudinal evolution of i_c at the maximum of the mean concentration field for both heavy and passive scalar emissions. In both cases, i_c raises, reaches a peak and decreases, and the heavy gas plume is characterised by lower fluctuation intensity in the far field. In the near field, the presence of CO_2 reduces therefore the intensity of the fluctuations, compared to the passive scalar. Indeed, the density difference affects the concentration field increasing its mean values and reducing the standard deviation.

As discussed by Nironi et al. (2015), once assumed that the PDF of the concentration can be well modelled by a Gamma distribution of the form:

$$p(\chi) = \frac{k^k}{\Gamma(k)} \chi^{k-1} \exp\left(-k\chi\right), \tag{14}$$

where $\Gamma(k)$ the Gamma function, $k = i_c^{-2}$ and $\chi \equiv c/\overline{c}$, we can retrieve a direct link between the value of k (and therefore i_c) and the form of the PDF.

In Fig. 7 we report five plots of one-point concentration PDF, together with a 5 s sample of the corresponding concentration signal. These five PDFs are obtained from measurements performed at the elevation where the maximal mean concentration occurs. The corresponding value of i_c, for increasing distance from the source, are indicated in Fig. 7a. Closer to the source, where the meandering motion is intense, the intermittency of the signal is high, therefore $i_c > 1$ (Fig. 7b) and the PDF follows an exponential-like distribution. As the plume grows and evolves, the meandering motion is gradually suppressed, the intermittency is reduced, i_c reaches the unit and the PDF is in transition between the exponential shape and the log-normal (Fig. 7c). In the far field, the relative dispersion becomes the only mechanism controlling turbulent transfer, i_c is below one and the intermittence of the signal is suppressed (Fig. 7d). Exception made by the very near field(Fig. 7f), where the concentration PDFs are directly affected by the dynamics of the vertical jet imposed at the emission, these results show that the Gamma distribution is suited to model, with good accuracy, the changing in

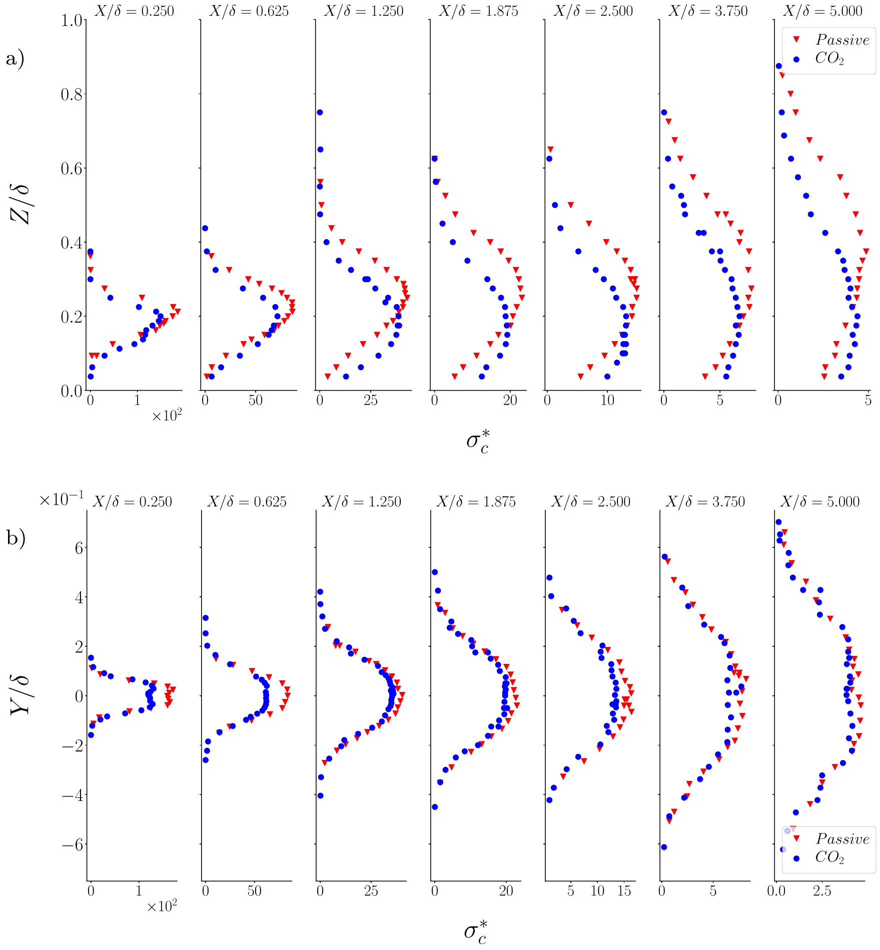

Fig. 6 Vertical **a** and transverse **b** profiles of the normalised standard deviation for sections at increasing distance from the source for passive and heavy gas plume

shape of PDF induced with increasing distance from the source by the turbulent dispersion within an atmospheric boundary layer, for both heavy and passive plume. (Fig. 7b–e).

A further proof of the reliability of the Gamma distribution as a model for the one-point concentration PDF is provided by the comparison between the 3rd and 4th order moments estimated from the measurements (Eq. 7) to the corresponding moments of the Gamma distribution, estimated as a function of the standard deviation as (Krishnamoorthy 2006):

$$m^*_{3c\Gamma} = \left(\frac{2}{\sqrt{k}}\right)^{1/3} \sigma^*_c, \tag{15}$$

$$m^*_{4c\Gamma} = \left(\frac{6}{k} + 3\right)^{1/4} \sigma^*_c. \tag{16}$$

The comparison is presented in Figs. 8 and 9, where we report the vertical and transverse profile of third- and fourth-order concentration statistics, for both passive scalar and heavy

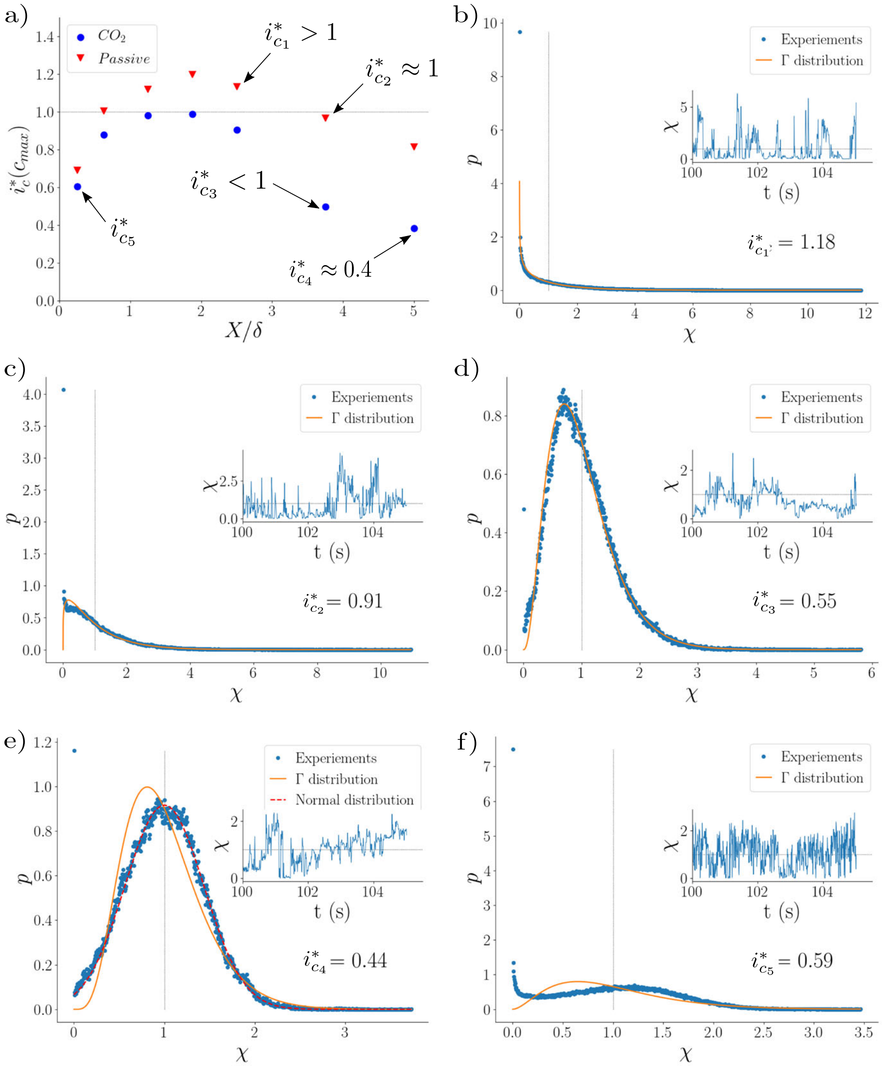

Fig. 7 Analysis of the relation of concentration PDF and fluctuation intensity i_c. **a** Longitudinal profile of the intensity of concentration fluctuation i^*_c for both heavy gas and passive scalar. Concentration PDF and signal sample for **b** $i^*_{c_1} > 1$ in the middle field, **c** $i^*_{c_2} \approx 1$, **d** $i^*_{c_3} < 1$ and **e** $i^*_{c_4} \approx 0.4$ in the far field, and **f** $i^*_{c_5} < 1$ near the source

gas, over a section in the near ($X = 0.625\delta$) and in the far field ($Z = 5\delta$). As for σ^*_c the presence of a heavy gas affects the high order moments, which are significant lower compared to the passive scalar plume, especially in the near field (Figs. 8a, b, and 9a, b). In the far field (Figs. 8c, d and 9c, d), the values of m^*_{3c} and m^*_{4c} decrease of almost two orders of magnitude. The larger discrepancies between the predictions provided by the Gamma distribution (as a function on the values of first- and second- order moments evaluated experimentally) and the experimental data is observed close to the source, where the velocity field and the concentration fluctuations are highly influenced by the momentum flux emitted at the

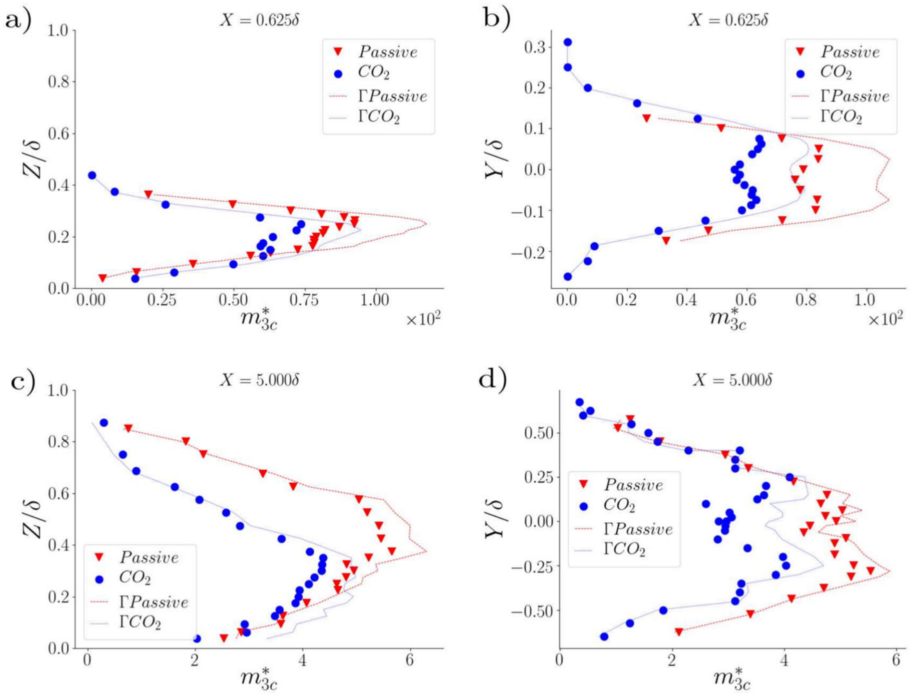

Fig. 8 3rd order moment: **a** vertical and **b** transverse profiles near the source ($X = 0.625\delta$) and **c** vertical and **d** transverse profiles in the far field ($X = 5\delta$), for a passive scalar and a heavy gas, compared with the moments obtained from the Gamma distribution models

chimney. In the far field, concentration moments estimated by Eqs. 15 and 16 show a good agreement with the experimental data. These results align with recent findings by Cassiani et al. (2024), who studied the release of a passive scalar in a turbulent boundary layer using Large Eddy Simulations. According to Cassiani et al. (2024), very near the source, where large-scale plume motion is most pronounced (Gifford 1959), the concentration PDF is only partially described by the Gamma distribution and is better captured by a meandering PDF. In the far field (Fig. 7e), as pointed out by Nironi et al. (2015), the concentration PDF transitions to a normal distribution at larger values of i_c than those predicted by the Gamma distribution, even though this shift aligns with the expected behaviour as i_c decreases. This feature has relevant practical implications for both by analytical (Bertagni et al. 2019) or Lagrangian (Marro et al. 2018) dispersion models, since it allows for the estimate of higher order statistics based on the evaluation of the mean and the standard deviation, only.

Despite substantial evidence supporting the reliability of the Gamma distribution as a one-point concentration PDF, no theoretical explanation has been established, to the best of our knowledge. The only attempt to derive it based on physical principles was made by Yee et al. (1993). Using a heuristic approach, they demonstrated that the Gamma distribution could be obtained from statistical arguments by assuming a Poisson distribution for the probability of finding effluent parcels in a sampling volume.

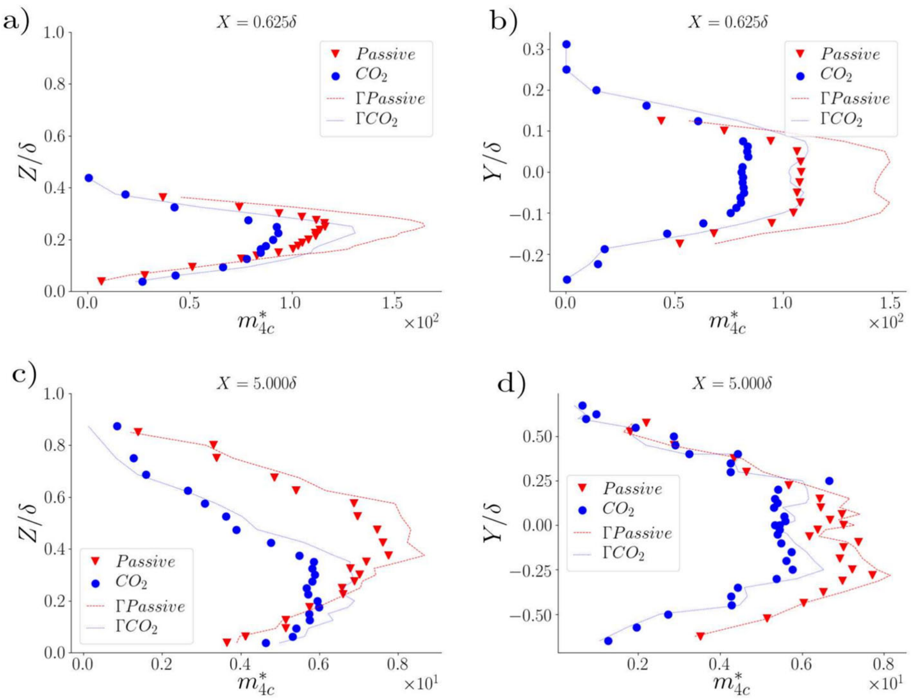

Fig. 9 4th order moment: **a** vertical and **b** transverse profiles near the source ($X = 0.625\delta$) and **c** vertical and **d** transverse profiles in the far field ($X = 5\delta$), for a passive scalar and a heavy gas, compared with the moments obtained from the Gamma distribution models

3.3 Turbulent Mass Fluxes

Simultaneous measurements of concentration and velocity allow us to compute profiles of turbulent mass fluxes at increasing distance from the source. The vertical profiles of horizontal turbulent mass fluxes $\overline{u'c'}^*$ are reported in Fig. 10a and vertical profiles of $\overline{w'c'}^*$ in Fig. 10b. The intensity of both $\overline{u'c'}^*$ and $\overline{w'c'}^*$ decreases with increasing distance from the source, as the plume spreads. The main difference between the two (dense and passive) plumes is a vertical shift of the profiles, due to the overall effect of buoyancy on the plume's centre of mass. Despite this shift, the profiles of the two plumes do not exhibit major differences. Notably, the maximal (absolute) value of the fluxes is almost unaffected by buoyancy. The only differences are detected very close to the source, where the maximum value for the dense release is slightly lower than that for the passive releases. This difference, however, is moderate, confirming that the role of negative buoyancy is more significant on the plume's elevation and trajectory than on the magnitude of the turbulent fluxes and their vertical profiles.

Adopting a standard gradient closure model:

$$\overline{w'c'^*} = -D_t^* \frac{\partial \overline{c^*}}{\partial z^*}, \tag{17}$$

experimental profiles $\overline{w'c'}^*$ and c^* have been exploited to evaluate vertical profiles of turbulent diffusion D_t^* (see Fig. 10c), and subsequently of the turbulent Schmidt number (Fig. 10d),

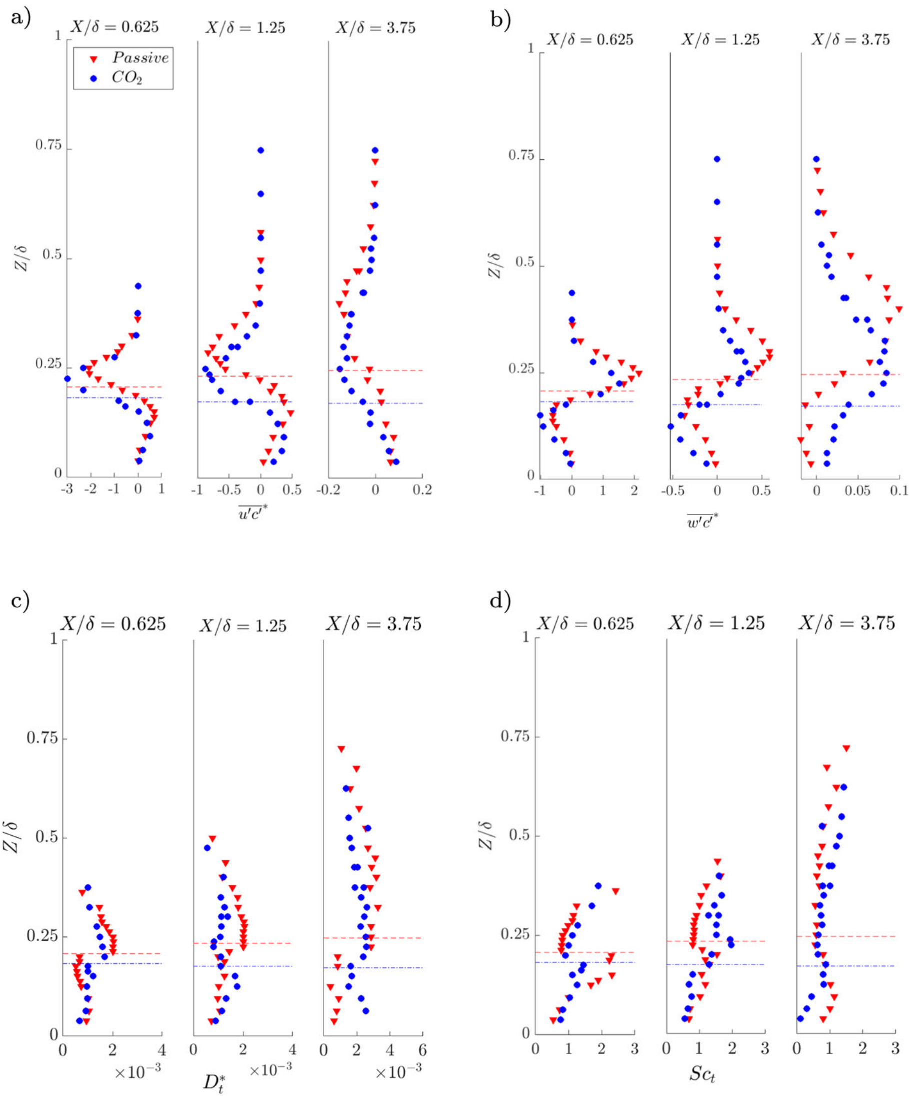

Fig. 10 Vertical profiles of the normalised **a** vertical and **b** horizontal turbulent mass flux, **c** turbulent diffusivity D_t^*, and **d** turbulent Schmidt number Sc_t for sections at increasing distance from the source for passive and heavy gas plume. The red and blue dashed lines represent the position of the centre of mass of the passive scalar and of the dense gas, respectively

$Sc_t = \frac{\nu_t^*}{D_t^*}$, where the turbulent viscosity is estimated as $\nu_t^* = \overline{u'w'}^* / \frac{\partial \overline{u}^*}{\partial z^*}$. As shown in Fig. 10c, the experimental estimates of D_t^* in the near field exhibit a discontinuity at the plume centreline, where gradients of the mean concentration are null. These discontinuities are due to slight uncertainties in the estimates of the low values of $\overline{w'c'^*}$ and $\frac{\partial \overline{c^*}}{\partial z^*}$, and they progressively fade with increasing distance from the source. Similar scatter in the near field is also observed in the vertical profiles of Sc_t, making it difficult to physically interpret the variation observed over the vertical coordinate. The more instructive profiles are those

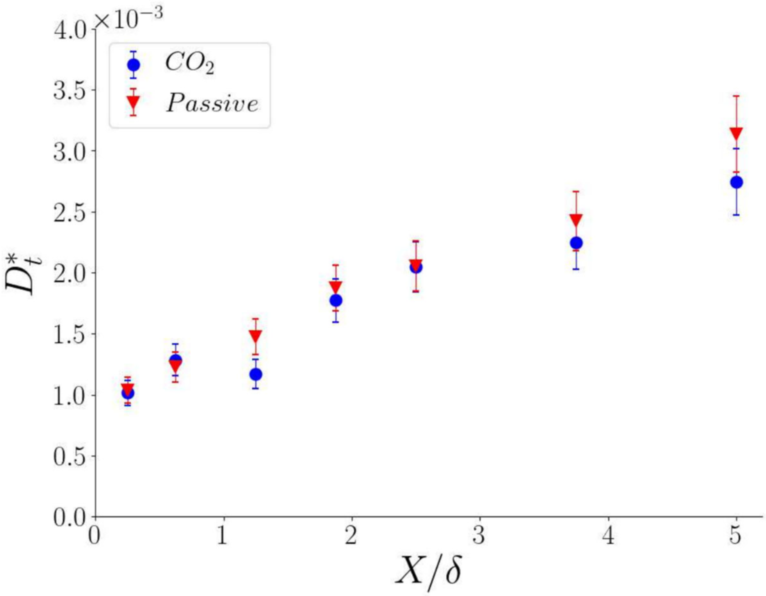

Fig. 11 Longitudinal profiles of the normalised turbulent dispersion factor D_t^* for both heavy gas and passive scalar plumes

evaluated at the farthest distance from the source ($X/\delta = 3.75$), showing values of Sc_t that are generally below unity in the core of the plume and slightly larger on the borders.

To filter out the experimental uncertainties and obtain a general view of the plume dynamics, it is useful to estimate a bulk turbulent diffusivity:

$$<D_t^*> = \frac{\int_0^\infty (\frac{\partial c^*}{\partial z^*}\overline{w'c'}^*)dz^*}{\int_0^\infty (\frac{\partial c^*}{\partial z^*})^2 dz^*}, \tag{18}$$

and analyse its longitudinal evolution. As evidence in Fig. 11, this shows an increasing trend with the distance from the source. This trend goes with the increasing size of the plume that, interacting with lager turbulent eddies, induces a more effective turbulent dispersion. We observe that there is no significant difference between a passive and a heavy gas emission. As for σ_z^*, the profile of the turbulent dispersion coefficient suggests that vertical dispersion is not influenced by buoyancy effects, whereas the plume trajectory clearly is.

The slight differences in plume spreads and eddy diffusivities between dense and passive scalars observed here can be attributed to the rapid transition from the slumping phase to the passive phase (Britter 1989; Heidorn et al. 1992). For releases with larger density differences, however, we would expect notable changes in plume behaviour and statistical properties. Notably, when the density difference arises from the release of solid particles, Csanady (1963) found that the fall velocity reduces eddy diffusivity, thereby limiting turbulent dispersion. Specifically, the presence of a drift velocity introduces a trajectory-crossing effect, causing particles to disperse more slowly than fluid elements (Aiyer and Meneveau 2022; Shende et al. 2024).

3.4 Production and Dissipation of Concentration Variance

In steady conditions, the balance equation of the concentration variance σ_c^2 for a high Reynolds number scalar release reads (Batchelor 1959; Csanady 1967):

$$-\frac{\partial}{\partial x_j}\left(\overline{u_j}\sigma_c^2 + \overline{u'_j c'^2}\right) - P - \varepsilon_{\sigma_c^2} = 0 \tag{19}$$

where the terms under the divergence operator are fluxes of concentration variance, due to the mean and fluctuating velocities, respectively, $P = -2\overline{u'_j c'}\frac{\partial \overline{c}}{\partial x_j}$ denotes the production term and $\varepsilon_{\sigma_c^2} = 2D\overline{\frac{\partial c'}{\partial x_j}\frac{\partial c'}{\partial x_j}}$ the dissipation rate. Quantifying the latter term is crucial in order to predict the local mixing induced by the atmospheric turbulence (Cassiani et al. 2020). Its experimental estimate is however challenging, since it requires the evolution of the gradients of the instantaneous concentration field. Its estimate has therefore to rely on alternative strategies. A first estimate can be achieved assuming the Taylor's hypothesis of frozen turbulence and the isotropic approximation as (Raupach and Legg 1983; Germaine et al. 2014):

$$\varepsilon_{\sigma_c^2 iso} = \frac{6D}{\overline{u}^2}\overline{\left(\frac{\partial c'}{\partial t}\right)^2}. \tag{20}$$

A second estimate relies on the analysis of the spectra of the concentration signal. For that, we assume a relation between the spectra and the dissipation of the concentration variance for the inertial sub-range of the form (Fackrell and Robins 1982):

$$PSD_v = \alpha_c \cdot 2\varepsilon_{\sigma_c^2 sp} \cdot \varepsilon_{iso}^{\frac{1}{3}} \cdot v^{-\frac{5}{3}}, \tag{21}$$

where v is the wave-number, ε_{iso} is the rate of dissipation of turbulent kinetic energy (Eq. 6) and $\alpha_c = 0.5$ is a constant (Warhaft 2000).

Profiles of $\varepsilon_{\sigma_c^2}$ are reported in Fig. 12, for both heavy gas and passive scalar, at three different distances from the source, together with estimates of the production rate of the concentration variance P. In the near field, where the effect of the source injections of momentum and concentration lead to higher gradient of velocity and concentration, P and $\varepsilon_{\sigma_c^2}$ have the same magnitude. Moving away from the source, both terms decrease by more of three orders of magnitude. Nevertheless, P decreases more rapidly than $\varepsilon_{\sigma_c^2}$. Notably, the vertical profiles of $\varepsilon_{\sigma_c^2}$, obtained with the two different methods show remarkable agreement one to the other (Fig. 12), with slight discrepancies that can be detected only in the very near field (Fig. 12a).

3.5 Mixing Time Scale

In evaluating the effect of the small scale turbulence on the dissipation rate of concentration variance, a key parameter is the so-called 'mixing time', whose parameterisation has to be included in analytical and stochastic models aiming at estimating the higher order moments of the concentration PDF (Marro et al. 2018; Bertagni et al. 2019; Cassiani et al. 2020).

The mixing time scale, referred here to as τ_m, represents the typical decay rate at which the dissipative action of small scale eddies tends to erase the inhomogeneities of the concentration field. In its simplest formulation, in the so-called 'interaction with the mean' (IEM) models,

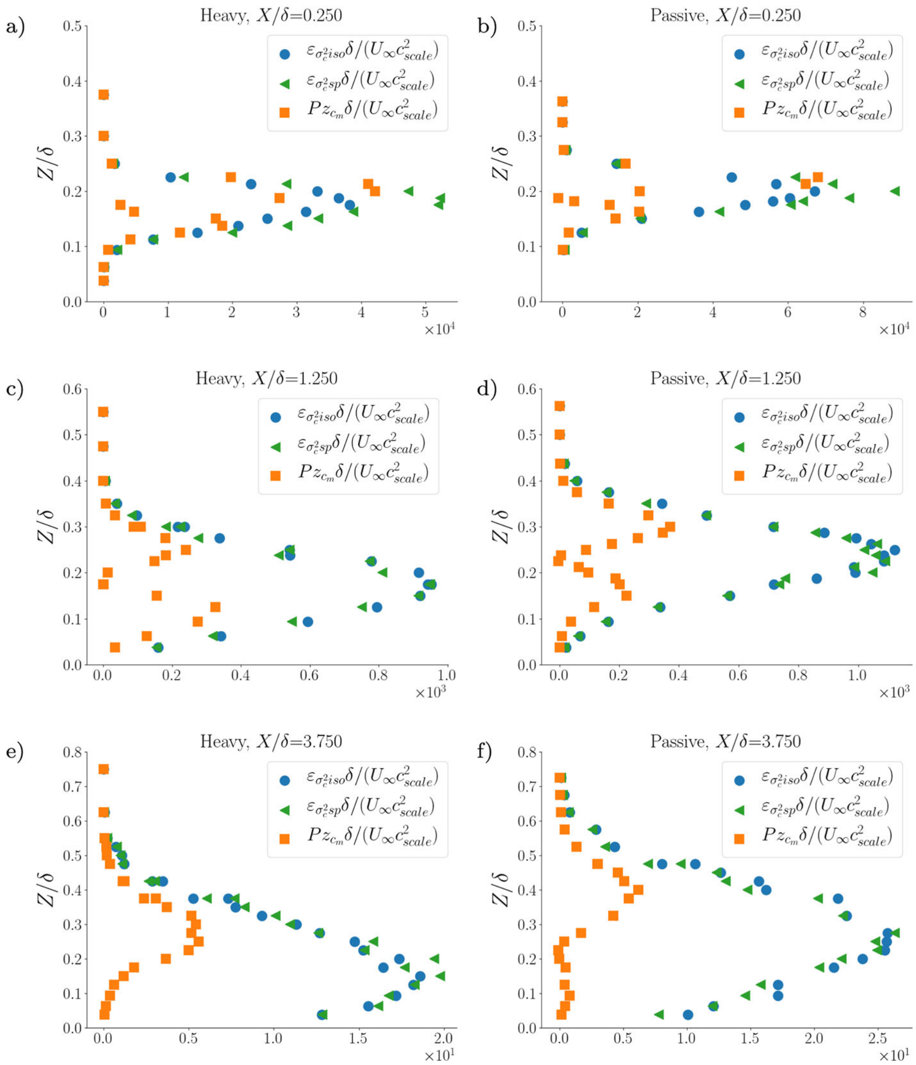

Fig. 12 Vertical profiles of the production and dissipation rate (P and σ_c^2) of concentration variance σ_c^2, estimated with two different methods, at increasing distance from the source for both (**a**, **c**, **e**) heavy gas, and (**b**, **d**, **f**) passive scalar plume

it is therefore linked to the concentration variance as:

$$\tau_m(IEM) = \tau_{m_c} = -\frac{\sigma_c^2}{\varepsilon_{\sigma_c^2}}. \tag{22}$$

A more complex parameterisation, referred to as 'interaction with the conditional mean' (IECM), can be instead achieved including also a term representing the meandering of the plume, through a mean concentration conditioned on the value of the local velocity $\langle c|u\rangle$. In this parameterisation the mixing time scale is expressed as (Cassiani et al. 2005):

$$\tau_m(IECM) = \tau_{m_{c|u}} = -\frac{1}{\varepsilon_{\sigma_c^2}}\left(\sigma_c^2 - \overline{c' \langle c|u\rangle}\right). \tag{23}$$

Note that, when $\langle c|u\rangle$ tends to $\overline{c}$ and the mean concentration is no-longer linked to any particular class of the velocity vector (implying that the larger scale structure of the flow does not have an influence on the variance generation) the two models are identical one to the other. In dispersion models (Marro et al. 2018), the value of τ_m is parameterised as a function of velocity statistics, and generally assumed to be a function of the distance from the source, only (i.e. independent of z). Among others, we focus here a model for micro-mixing time $\tau_{m_{mod}}$ presented by Cassiani et al. (2005):

$$\tau_{m_{mod}} = \mu_t \frac{\sigma_r}{\sigma_{ur}}, \tag{24}$$

where $\mu_t = 0.44$ is an empirical constant (Marro et al. 2018), σ_r is the relative plume spread around the plume's centroid and σ_{ur} is the r.m.s. of the relative velocity fluctuations, parametrised as:

$$\sigma_{ur}^2 = \sigma_u^2 \left(\frac{\sigma_r}{L}\right)^{2/3}, \tag{25}$$

where $L = \frac{(3\sigma_u^2/2)^{3/2}}{\varepsilon}$ is an estimate of the Eulerian integral length scale (Sawford and Stapountzis 1986). Note that, as far as $\sigma_r > L$, i.e. when the plume meandering is negligible, the whole TKE contributes to the relative dispersion, i.e. $\sigma_{ur} = \sigma_u$. The relative plume spread is evaluated as:

$$\sigma_r^2 = \frac{d_r^2}{1 + (d_r^2 - d_s^2)/(d_s^2 + 2\sigma_u^2 T_L t)}, \tag{26}$$

where:

$$d_r^2 = C_r \varepsilon (t_0 + t)^3, \tag{27}$$

where $t_0 = (d_s^2/C_r\varepsilon)^{1/3}$ is the inertial formulation for a dispersion from a finite source size d_s (with $C_r = 0.3$) (Franzese 2003), and the Lagrangian time scale is evaluated according to Eqs. 12 and 13.

Our aim here is that of discussing experimental estimates of the micro-mixing time scale τ_m (as well as of the typical turbulent time scale $\tau = K/\varepsilon$) and compare these with the estimate $\tau_{m_{mod}}$ provided by the model, i.e. Eqs. 24–27.

As a first step, we focus on the vertical variability of the mixing time. Figure 13 shows the vertical profiles of τ_{m_c}, $\tau_{m_{c|u}}$ and τ at increasing distance from the source. In presenting the data, we only plot those relative to the heavy release, that however do not show any relevant discrepancy with those obtained considering the passive release. For sake of clarity we reported the micro-mixing time scale estimated in the core of the plume, i.e. only for $Z_{MC} - 2\sigma_z < z < Z_{MC} + 2\sigma_z$. Over the vertical plume section, estimates of τ_m exhibit a clear increasing trend, which is attenuated for increasing distances from the source. As discussed by Amicarelli et al. (2012), the IEM model is expected to overestimate the variance dissipation compared to the IECM model, which would imply $\tau_{m_c} < \tau_{m_{c|u}}$. Our results show however very similar estimates provided by $\tau_{m_{c|u}}$ and τ_{m_c} throughout the whole plume section, with differences between the two that cannot be dissociated from our experimental uncertainties.

As a second step, we analyse longitudinal profiles of τ_m (we assume hereafter no difference between τ_{m_c} and $\tau_{m_{c|u}}$) and $\tau_{m_{mod}}$ as estimated at the plume centre of mass. The results,

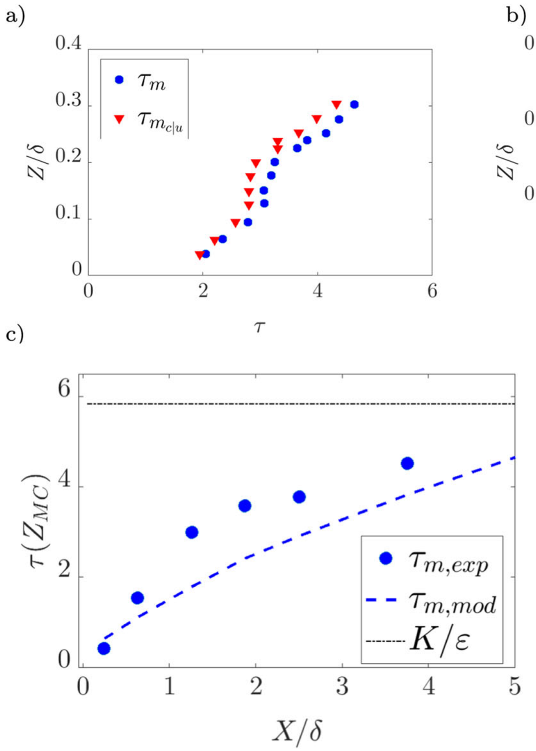

Fig. 13 Mixing time of dense gas estimated with two different models (IEM, IECM): **a** vertical profile at $X = 1.25\delta$, **b** vertical profile at $X = 5.0\delta$. **c** Longitudinal profile of the mixing time $\tau_{m,exp}$ compared with the micro-mixing model $\tau_{m,mod}$ (Eq. 24), see Cassiani et al. (2005)

reported in Fig. 13c, show that the estimates of the model $\tau_{m_{mod}}$ nicely reproduce the increasing trend of τ_m depicted by the experimental estimates, with a tendency of underestimating the experimental data in the intermediate field. As evidenced in Fig. 13c, both modelled and experimental estimates progressively tend to the value of turbulent time scale $\tau = K/\varepsilon$, which is usually considered as the asymptotic limit of τ_m in the far field (Marro et al. 2018).

4 Conclusions

In this study, we analysed the dynamics of the turbulent dispersion of a heavy gas and a passive scalar released from an elevated source within a turbulent boundary layer. We characterised the pollutant plumes downwind of the source by simultaneously measuring the concentration and velocity fields using a system coupling a Hot-Wire Anemometer with a Flame Ionization Detector (HWA-FID). The vertical profiles of the mean concentration show significant differences between the two cases analysed. To quantify these differences, we used the mean concentration profiles to estimate the height of the centre of mass Z_{MC} and the vertical and transverse plume spread, σ_z and σ_y, respectively.

The results highlight the role of buoyancy in deflecting the plume centre of mass and causing its impact closer to the source (compared to the passive case). Interestingly, however, the plume spread is almost insensitive to the presence of buoyancy. Simultaneous measurements of concentration and velocity allowed us to obtain vertical profiles of vertical and longitudinal turbulent mass fluxes, respectively $\overline{w'c'}$ and $\overline{u'c'}$. These profiles were subsequently used to estimate turbulent dispersion coefficients and the turbulent Schmidt number. Except very close to the source, where the velocity and concentration fields are directly affected by the vertical jet imposed at the release, no major differences were observed between the dense and passive plumes.

Similarly, the effect of buoyancy on higher-order concentration statistics diminishes rapidly with distance from the source. As with passive scalar releases, the one-point concentration statistics of the dense gas plume are well modelled by a Gamma distribution and can therefore be predicted through the estimate of the fluctuation intensity $i_c = \sigma_c^* / \overline{c^*}$.

Finally, we analysed the spatial distribution of the production of concentration variance and its dissipation rate, which allowed us to quantify typical mixing time scales τ_m of the flow. This enabled us to evaluate the reliability of the parameterization of the mixing time usually adopted in atmospheric dispersion models.

To summarise, the experimental results show that negative buoyancy at the source significantly affects only the mean concentration field, as the trajectory of the plume centre of mass is deflected toward the ground. Plume spread and higher-order concentration statistics are largely unaffected by buoyancy, except in the very near-field region. These findings have major implications for the development of operational dispersion models used to simulate localised dense gas emissions.

Funding Open access funding provided by École Centrale de Lyon.

Appendix

We report here the scalar PDFs analysed in Fig. 7 represented in log-scale in order to highlight as the Gamma distribution allows the extreme values to be described. Figure 14 shows that the Gamma distribution reproduces the experimental PDFs in the intermediate scalar field, for both low and high values, with a remarkable accuracy (Fig. 14a–c). In the very far field, the concentration PDF approaches a normal distribution (Fig. 14d), as noted in Nironi et al. (2015). In the region where the meandering is dominant, namely very close to the source location, the Gamma distribution presents lower accuracy in describing the scalar statistics and the meandering PDF provides a better agreement (Cassiani et al. 2024).

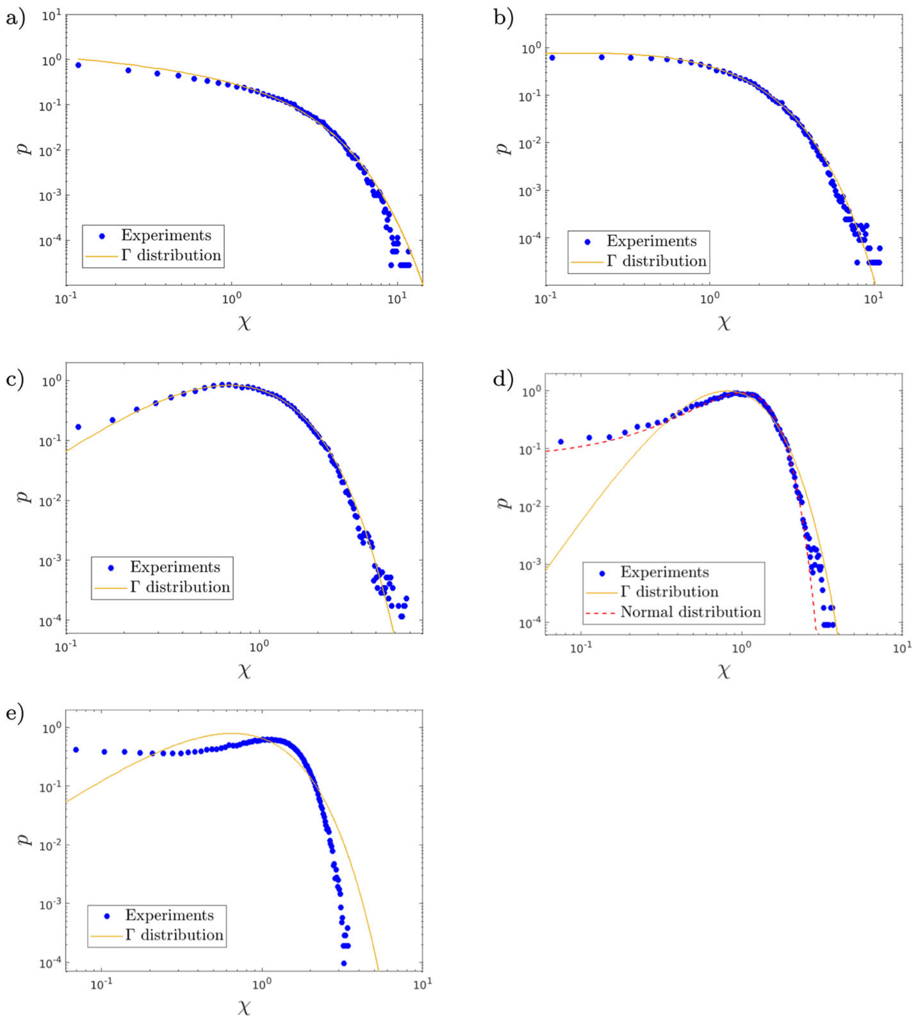

Fig. 14 Analysis of the experimental scalar PDF in log scale for different values of the parameter i_c, as in Fig. 7: **a** $i^*_{c1} = 1.18$, **b** $i^*_{c2} = 0.91$, **c** $i^*_{c3} = 0.55$, **d** $i^*_{c4} = 0.44$, **e** $i^*_{c5} = 0.59$

References

Aiyer A, Meneveau C (2022) Resolved and subgrid-scale crossing trajectory effects in Eulerian large eddy simulations of size-dependent droplet transport. J Fluid Mech 935:A15

Amicarelli A, Leuzzi G, Monti P (2012) Lagrangian micromixing models for concentration fluctuations: an overview. AJES 8(6):577–590

Arya S, Lape J (1990) A comparative study of the different criteria for the physical modeling of buoyant plume rise in a neutral atmosphere. Atmos Environ A Gen Top 24(2):289–295

Ayrault M, Balint JL, Morel R (1991) An experimental study on the evolution and dispersion of a cloud of gas heavier than air. J Hazard Mater 26(1):1–26

Ayrault M, Simoëns S, Méjean P (1998) Negative buoyancy effects on the dispersion of continuous gas plumes downwind solid obstacles. J Hazard Mater 57(1–3):79–103

Batchelor GK (1959) Small-scale variation of convected quantities like temperature in turbulent fluid part 1. General discussion and the case of small conductivity. J Fluid Mech 5(1):113–133

Bertagni MB, Marro M, Salizzoni P, Camporeale C (2019) Solution for the statistical moments of scalar turbulence. Phys Rev Fluids 4(124):701

Bertagni MB, Marro M, Salizzoni P, Camporeale C (2020) Level-crossing statistics of a passive scalar dispersed in a neutral boundary layer. Atmos Environ 230(117):518

Bodurtha FT (1961) The behavior of dense stack gases. J Air Pollut Control Associat 11(9):431–437

Briggs G, Britter R, Hanna S, Havens J, Robins A, Snyder W (2001) Dense gas vertical diffusion over rough surfaces and results of wind-tunnel studies. Atmos Environ 35:2265–2284

Britter RE (1989) Atmospheric dispersion of dense gases. Annu Rev Fluid Mech 21(1):317–344

Britter RE, Snyder WH (1988) Fluid modeling of dense gas dispersion over a ramp. J Hazard Mater 18(1):37–67

Cassiani M, Franzese P, Giostra U (2005) A pdf micromixing model of dispersion for atmospheric flow. Part I: development of the model, application to homogeneous turbulence and to neutral boundary layer. Atmos Environ 39(8):1457–1469

Cassiani M, Bertagni MB, Marro M, Salizzoni P (2020) Concentration fluctuations from localized atmospheric releases. Boundary-Layer Meteorol 177:461–510

Cassiani M, Ardeshiri H, Pisso I, Salizzoni P, Marro M, Stohl A, Stebel K, Park SY (2024) The dynamics of concentration fluctuations within passive scalar plumes in a turbulent neutral boundary layer. J Fluid Mech 1001:A18

Csanady G (1967) Concentration fluctuations in turbulent diffusion. J Atmos Sci 24(1):21–28

Csanady GT (1963) Turbulent diffusion of heavy particles in the atmosphere. J Atmos Sci 20(3):201–208

Donat J, Schatzmann M (1999) Wind tunnel experiments of single-phase heavy gas jets released under various angles into turbulent cross flows. J Wind Eng Ind Aerodyn 83:361–370

Fackrell JE, Robins AG (1982) Concentration fluctuations and fluxes in plumes from point sources in a turbulent boundary layer. J Fluid Mech 117:1–26

Franzese P (2003) Lagrangian stochastic modeling of a fluctuating plume in the convective boundary layer. Atmos Environ 37(12):1691–1701

Germaine E, Mydlarski L, Cortelezzi L (2014) Evolution of the scalar dissipation rate downstream of a concentrated line source in turbulent channel flow. J Fluid Mech 749:227–274

Gifford F (1959) Statistical properties of a fluctuating plume dispersion model. In: Advances in Geophysics, vol 6, Elsevier, pp 117 – 137

Hanna S, Steinberg K (2001) Overview of petroleum environmental research forum (perf) dense gas dispersion modeling project. Atmos Environ 35(13):2223–2229

Hanna SR, Chang JC (2001) Use of the kit fox field data to analyze dense gas dispersion modeling issues. Atmos Environ 35(13):2231–2242

Hay J, Pasquill F (1959) Diffusion from a continuous source in relation to the spectrum and scale of turbulence. Adv Geophys 6:345–365

Heidorn K, Murphy M, Irwin P, Sahota H, Misra P, Bloxam R (1992) Effects of obstacles on the spread of a heavy gas-wind tunnel simulations. J Hazard Mater 30(2):151–194

Hinze J (1975) Turbulence. McGraw-Hill, New York, p 799

Hoot T, Meroney R, Peterka J (1973) Wind tunnel tests of negatively bouyant plumes[final report]. Final Report

Irwin H (1981) The design of spires for wind simulation. J Wind Eng Ind Aerodyn 7(3):361–366

Krishnamoorthy K (2006) Handbook of statistical distributions with applications. Chapman and Hall/CRC, Boca Raton

König-Langlo G, Schatzmann M (1991) Wind tunnel modeling of heavy gas dispersion. Atmos Environ A Gen Top 25(7):1189–1198

Marro M, Salizzoni P, Cierco FX, Korsakissok I, Danzi E, Soulhac L (2014) Plume rise and spread in buoyant releases from elevated sources in the lower atmosphere. Environ Fluid Mech 14:201–219

Marro M, Salizzoni P, Soulhac L, Cassiani M (2018) Dispersion of a passive scalar fluctuating plume in a turbulent boundary layer. Part III: stochastic modelling. Boundary-Layer Meteorol 167(3):349–369

Marro M, Gamel H, Méjean P, Correia H, Soulhac L, Salizzoni P (2020) High-frequency simultaneous measurements of velocity and concentration within turbulent flows in wind-tunnel experiments. Exp Fluids 61(12):245

Meroney RN (1982) Wind-tunnel experiments on dense gas dispersion. J Hazard Mater 6(1):85–106

Meroney RN, Lohmeyer A (1984) Statistical characteristics of instantaneous dense gas clouds released in an atmospheric boundary-layer wind tunnel. Boundary-Layer Meteorol 28(1):1–22

Nironi C, Salizzoni P, Marro M, Mejean P, Grosjean N, Soulhac L (2015) Dispersion of a passive scalar fluctuating plume in a turbulent boundary layer. Part I: velocity and concentration measurements. Boundary-Layer Meteorol 156(3):415–446

Raupach MR, Legg BJ (1983) Turbulent dispersion from an elevated line source: measurements of wind-concentration moments and budgets. J Fluid Mech 136:111–137

Roberts P, Hall D (1994) Wind-tunnel simulation. Boundary layer effects in dense gas dispersion experiments. J Loss Prev Process Ind 7(2):106–117

Robins A, Castro I, Hayden P, Steggel N, Contini D, Heist D (2001a) A wind tunnel study of dense gas dispersion in a neutral boundary layer over a rough surface. Atmos Environ 35(13):2243–2252

Robins A, Castro I, Hayden P, Steggel N, Contini D, Heist D, Taylor TJ (2001b) A wind tunnel study of dense gas dispersion in a stable boundary layer over a rough surface. Atmos Environ 35(13):2253–2263

Sawford BL, Stapountzis H (1986) Concentration fluctuations according to fluctuating plume models in one and two dimensions. Boundary-Layer Meteorol 37(1):89–105

Schatzmann M, Snyder WH, Lawson RE (1993) Experiments with heavy gas jets in laminar and turbulent cross-flows. Atmos Environ A Gen Top 27(7):1105–1116

Shende OB, Storan L, Mani A (2024) A model for drift velocity mediated scalar eddy diffusivity in homogeneous turbulent flows. J Fluid Mech 989:A14

Snyder WH (2001) Wind-tunnel study of entrainment in two-dimensional dense-gas plumes at the EPA's fluid modeling facility. Atmos Environ 35(13):2285–2304

Taylor GI (1922) Diffusion by continuous movements. Proc Lond Math Soc 2(1):196–212

Tennekes H, Lumley JL (1972) A first course in turbulence. MIT Press, Cambridge

Vidali C, Marro M, Correia H, Gostiaux L, Jallais S, Houssin D, Vyazmina E, Salizzoni P (2022) Wind-tunnel experiments on atmospheric heavy gas dispersion: Metrological aspects. Exp Thermal Fluid Sci 130(110):495

Warhaft Z (2000) Passive scalars in turbulent flows. Annu Rev Fluid Mech 32(1):203–240

Yee E, Kosteniuk P, Chandler G, Biltoft C, Bowers J (1993) Statistical characteristics of concentration fluctuations in dispersing plumes in the atmospheric surface layer. Boundary-Layer Meteorol 65(1–2):69–109

Zhu G, Arya S, Snyder WH (1998) An experimental study of the flow structure within a dense gas plume. J Hazard Mater 62(2):161–186